Revista Mexicana de Astronomía y Astrofísica, 61, 142-153, (2025)

OPEN ACCESS https://doi.org/10.22201/ia.01851101p.2025.61.03.03

Analysis of Telescope-Detector Coupling for a Mid-Infrared Solar Flare Observations Telescope

J. S. Palacios-Fonseca [1], **J. E. Mendoza-Torres** [2] **and M. Velázquez** [2]

[1]*Unidad Académica de Ciencias Básicas e Ingenierías (UACBI), Universidad Autónoma de Nayarit, México.*
[2]*Instituto Nacional de Astrofísica, Óptica y Electrónica, Departamento de Astrofísica, México.*

Keywords: *Infrared: general, Instrumentation: detectors, Sun: infrared, Telescopes*

Abstract

This study analyzes various optical couplings between an RC telescope and an MIR detector to develop a portable instrument for solar observation. The coupling systems included lenses or mirrors –custom-made and catalog types–, as well as direct coupling analysis. Simulations of the couplings were performed using the Zemax package to estimate the ray dispersion, Airy disk diameter, and PSF. Coupling with catalog lenses shows better performance, and their FOV allows the observation of a region as wide as the solar diameter. Direct coupling provides a higher spatial resolution for resolving smaller solar active regions, although it has a smaller FOV than indirect coupling. Therefore, depending on the observation goal on the Sun, the telescope can operate with either optical coupling configuration to cover a larger or smaller area on the solar disk.

Resumen

Este trabajo analiza varios acoplamientos ópticos entre un telescopio RC y un detector MIR con el objetivo de desarrollar un instrumento portátil para la observación solar. Los sistemas de acoplamiento incluyen lentes o espejos, tanto de tipo personalizado como de catálogo, y se analiza el acoplamiento directo. Se realizan simulaciones de los acoplamientos con el programa Zemax para estimar la dispersión de rayos, el diámetro del disco de Airy y la PSF, entre otros. El acoplamiento con lentes de catálogo muestra un mejor desempeño y su campo de visión permitirá la observación de una región tan amplia como el diámetro solar. El acoplamiento directo provee mayor resolución espacial para resolver regiones de actividad solar pequeñas, aunque con un campo de visión más pequeño. Por lo tanto, dependiendo del objetivo de observación en el Sol, el telescopio puede operar con cualquiera de los acoplamientos para cubrir un área mayor o menor en el disco solar.

Corresponding author: J. S. Palacios-Fonseca *E-mail address:* juan.palacios@uan.edu.mx
Received: December 29, 2023 **Accepted:** August 6, 2025

1. Introduction

For several centuries, the Sun has been observed with telescopes in the visible range of the electromagnetic spectrum, and for more than half a century, it has been observed at meter, microwave, and centimeter wavelengths. Additionally, it has been observed in UV, X-rays, and other wavelengths for several decades. However, in the mid-infrared (MIR), the Sun has been observed little, and, to date, less than ten solar flares have been reported in the MIR, whereas in other wavelengths, even hundreds of flares are reported during a single month[1]. This is partly conditioned by atmospheric absorption (Qin et al., 2001; Giovanelli et al., 2001; Sobrino et al., 2004). Absorption depends on various factors, including the path length of the atmosphere. The longer the length, the lower the energy that reaches the Earth's surface from a cosmic object. Some astronomical facilities are installed at high altitudes to diminish the loss of energy received by telescopes on Earth (Hills & Richer, 2000; Giovanelli et al., 2001; Naylor et al., 2002; Otárola et al., 2010; García-Lorenzo et al., 2010). However, such facilities require extensive infrastructure and logistical support for both installation and maintenance, which increase in proportion to the size of the telescope.

Solar activity at mid-infrared wavelengths (including solar flares) has been investigated for decades. In the 1970s, for example,Turon & Léna (1970) used the McMath-Pierce Solar Telescope to record images at 10 μm with a microbolometer cooled to 2 K (Pierce, 1969). The obtained images showed small bright areas near the sunspots, particularly at the edge of the penumbra. In 1974, Hudson & Lindsey (1974) observed the Sun at 20 μm at the 60-inch diameter Mont Lemmon Infrared Observatory and found variations with a 300 s period. In 1981, Lindsey & Heasley (1981) used the 2.24 m telescope at the Mauna Kea Observatory and recorded faculae emissions at 10.5, 18, and 25 μm wavelengths. The first solar flare was observed in 2012 (Kaufmann et al., 2013) using the Leoncito Observatory telescope (Melo et al., 2006; Marcon et al., 2008; Kaufmann et al., 2008). Kaufmann's team (Kaufmann et al., 2012; Kaufmann et al., 2014) detected a solar flare with a telescope called Solar-T operating at 40 mm and 100 mm during a stratospheric balloon flight over Antarctica, and

[1]www.ngdc.noaa.gov/stp/solar/solarflares.html

one more in 2016 (Kaufmann et al., 2016). Judge et al. (2019) made spectroscopic observations in various electromagnetic spectrum bands (including the infrared, 0.295-1.10, 0.94-1.92, 0.95-2.50 and 1-5 μm) during the solar eclipse of August 21, 2017, with four spectrometers deployed at Camp Wyoba on Casper Mountain.A solar flare of magnitude X9 at 10 μm was observed by Giménez de Castro et al. (2018) using a 15 cm aperture Newtonian system.

Solar flares are transient events characterized by an increase in the flux at several wavelengths of the electromagnetic spectrum, along with the acceleration of particles. They have been described with observational and theoretical detail by Aschwanden (2006) and references therein. The flares last approximately one minute to one hour and occur in the Active Regions (ARs), which appear between +45 and -45 degrees of solar latitude across the solar disk. ARs are observed in the visible wavelengths as groups of dark spots. Each AR covers an area of a few arc-minutes (McIntosh, 1990). The number of spots and flares varies throughout the 11–year cycle of solar activity. A group of spots can last from a few days to several months. Around the maximum activity, a larger number of spots and flares were recorded. In contrast, the umber of flares recorded at different wavelengths increased as the energy decreased. Their number distribution concerning energy follows a power-law function with a slope $\lesssim 2$. It is believed that the flares may result from the release of magnetic energy, but this has not been confirmed. However, this phenomenon is of interest in the case of the Sun and other stars, where similar events occur (Forbes, 2000).

To observe solar flares, the field of view (FOV) of the telescope must cover the region of the solar disk where ARs appear. This implies that the FOV must be a few arc-minutes long. However, good spatial resolution is desirable for creating detailed maps of emission sources. To record the temporal evolution of emissions in ARs, it is advisable to have an image capture cadence at short time intervals, on the order of seconds or less. The thermal resolution of the telescope must allow the excess brightness temperature to be recorded during a solar flare, which could reach 25deg K (López et al., 2022) in the mid-infrared (MIR) range.

This work explains the optics of the MIR portable solar telescope, *Telescopio Solar Portátil para Mediano Infrarrojo*, *TSP-MIR*. The telescope is designed to observe solar emission in the 8 to 12 μm wavelength range. The FOV of the telescope covers wide regions of the solar disk, aiming to record the areas of one or several ARs in the process. An image capture cadence of up to four images per second allows for the observation of the temporal evolution of events on the solar disk. With data from the TSP-MIR, the recording of transient events and solar flares in ARs is intended to be increased in the future. The study of MIR emissions and observations at other wavelengths will allow for a better understanding of the energy transport mechanism during an eruptive event.

2. Design Criteria

This section outlines the design requirements of the proposed TSP-MIR. It considers the FOV necessary for the telescope to observe both individual and multiple ARs simultaneously. Additionally, it addresses the components of solar telescopes, including the type of telescope, infrared windows, detectors, and coupling systems.

2.1. Resolution, field of view, and integration time

ARs observed in the MIR have angular sizes ranging from arc-seconds to a few arc-minutes (Kaufmann et al., 2013; Giménez de Castro et al., 2018; López et al., 2022). An FOV that covers the entire solar disk increases the likelihood of observing all ARs present on the visible side of the Sun and registering more flares than a smaller FOV does. Considering that a detector has a limited number of elements, the larger the FOV, the lower the spatial resolution. However, the larger the FOV covered by a pixel, that is, the solid angle in the sky or on the solar disk, the more energy it captures.

Conversely, with a smaller FOV, a better spatial resolution is achieved, making it possible to obtain more detailed maps of the sources in ARs and study their spatial distributions. In this case, the optical configuration must not spread the energy from a point source over an area larger than the diffraction limit (i.e., an Airy disk). Additionally, this area should be equal to or smaller than the size of an individual pixel. The less dispersion a telescope produces, the more reliable the map will be, and consequently, the more accurate the identification of variations in the source's brightness. The captured energy was also lower, but more energy was received as the integration time increased. However, information on variations at shorter time scales is lost. For example, during the impulsive phase of a solar flare, the MIR emission changes in time intervals of a few seconds (Penn et al., 2016).

Therefore, a balance must be achieved between the angular resolution, FOV, and time intervals between the images recorded by the detector. For the TSP-MIR, two FOVs were considered that can be used at different times during solar observation. The first is an FOV no greater than 10 arc-min, with a better spatial resolution to resolve the structure of an individual AR. The second FOV was at least three times larger than the first one. This will allow the monitoring of two or more ARs on the solar disk in the future. The integration interval of each image is electronically controlled in the detector and varies from time intervals of $\tau = 0.25$ ms or longer.

2.2. Observation Requirements for the TSP-MIR

The TSP-MIR is designed as a portable instrument that can be deployed quickly at different sites. The incorporation of commercial optical and electronic components was chosen to reduce integration expenses. Additionally, this will allow the design to be replicated to have other telescopes that can monitor different ARs simultaneously, possibly at different wavelengths. The observation requirements selected for the solar telescope were as follows:

1. Two optical modes of operation are considered:
    a. High resolution, constrained by the diffraction limit in the 8 to 12 μm wavelength range, with a small FOV equivalent to an AR.
    b. The low resolution is constrained by the pixel size, with a large field of view equivalent to the angular diameter of the Sun.
2. A sampling rate of 1 image per second or higher is required.
3. Optical system aberrations that disperse the incident energy beyond the size of the Airy disk in the 8 to 12 μm wavelength range should be avoided as much as possible.
4. The energy flux must be limited to avoid detector saturation.

2.3. Detectors

Until a few years ago, MIR detectors required cryogenic systems for their operation. Currently, new detectors can operate at room temperature, eliminating the need for cryogenic systems. This is a major benefit of the new detectors compared to the older ones,

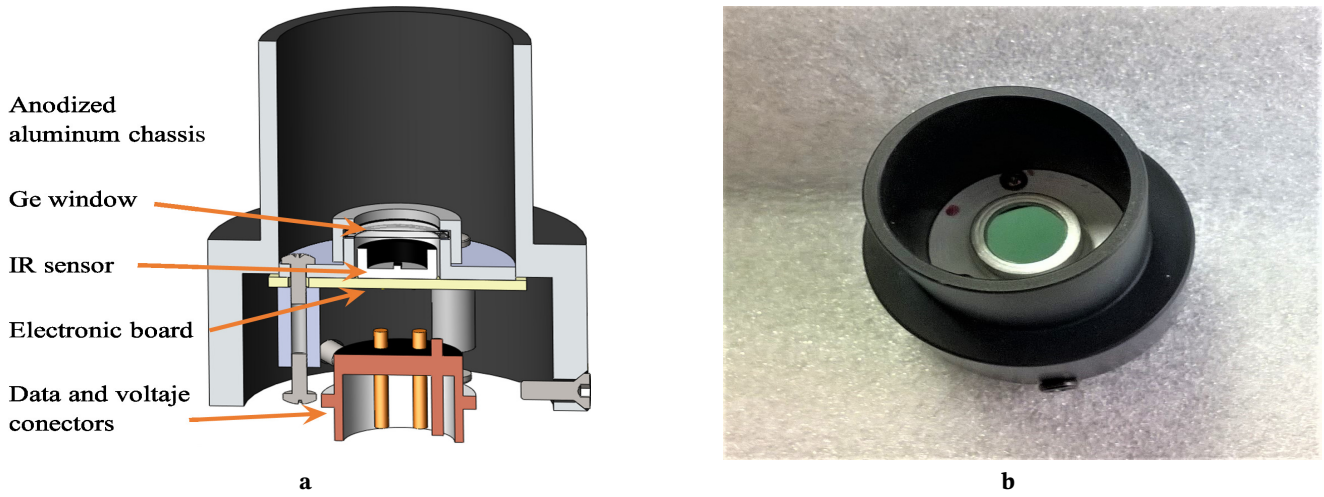

Figure 1. MIR detector module. (a) Schematic of detector integration into the chassis. (b) Prototype of the MIR detector module in an anodized aluminum chassis. The chassis had a standard diameter of 1.25 in. The MIR detector module can be installed in the place occupied by a conventional eyepiece, facilitating its coupling to a commercial telescope.

as the number of electronic and mechanical components can be reduced for an MIR telescope, and its design and construction can become easier, allowing the building of telescopes with low infrastructure requirements or portable telescopes for observation campaigns. For example, when an AR exhibits high activity, a telescope may be used to monitor it, allowing the possibility of observing flares. Inexpensive telescopes also allow multiple telescopes to observe different regions of the Sun. In this case, each telescope can cover an FOV of different sizes to cover the band where ARs occur or individual AR with better spatial resolution. In the case of more than one telescope, it would also allow observations at various wavelengths and polarizations to be made. In addition, in recent years, MIR detector arrays have been manufactured with more elements, and their prices have decreased, improving the possibility of building telescopes with better spatial resolution.

The MIR detector module for TSP-MIR was integrated with the MLX90620 device from Melexis, which has an array of 64 pixels distributed in 16 columns and four rows. Each pixel measured 0.23 mm per side. The complete pixel array was 3.68 mm in width and 0.92 mm in height, as shown in Table 1. The sampling rate of the detector can be configured to a maximum of 4 frames per second. The Noise Equivalent Temperature Difference (NETD) of the detector was 80 mK with a sampling rate of 1 frame per second. The NETD is the minimum detectable change in temperature by an individual pixel or the pixel thermal resolution, which is sufficient for detecting the excess brightness temperature of a solar flare. Figure 1(a) shows a schematic of the MIR detector module designed for the TSP-MIR. A germanium window was integrated into an aluminum chassis at a short distance from the Melexis pixel array.

Figure 1(b) shows the mechanical module of the MIR detector. The detector module chassis was fabricated using a 6061 aluminum alloy. It has a standard outer diameter of 1.25−inch in the section that attaches to the telescope and 44 mm in the section where the detector and electronic board are housed. The chassis has a matte black anodized finish to reduce light reflection inside the module. To maintain a stable temperature in the pixel array, thermal contact is maintained with the detector chassis through the ground plane of the electronic board where it was installed. Excess heat was dissipated in the telescope metal tube. Thermal equilibrium between the internal components of the tube and the exterior of the telescope was achieved shortly before the observation, preventing an internal temperature gradient that could cause local turbulence. The local temperature of the surrounding detector was monitored using an internal thermometer in the MLX90620. During preliminary tests, the internal temperature was maintained at stable values similar to the external environment of the telescope. The design of the MIR detector module as an eyepiece facilitates the replacement of the detector, either with another identical detector (in case it is damaged) or with a different type of detector.

Table 1. Array dimensions and pixel sizes.

Detector	Array	Size (mm)	Pixel size (mm)
Melexis	16×4	3.68×0.92	230

2.4. RC Telescope integration

To meet the requirements for the TSP-MIR, a Ritchey-Chretien (RC) telescope was selected because it operates based only on mirrors and consequently does not suffer from absorption losses in visible light. In addition, this type of telescope has a wider FOV than other configurations (Riedl, 2009), and its mirrors are hyperbolically shaped. It does not undergo spherical aberration or third-order coma, which occur in other telescope types. The RC telescope had an f/9 focal ratio and an aperture of 152 mm. Its optical resolution, given by the diffraction limit, is 16.6″for a wavelength of 10 μm. RC mirrors have low absorption owing to the SiO_2 coating, which protects the aluminum surface of the mirror. According to Kischkat et al. (2012) and Polyanskiy (2021), the absorption due to the SiO_2 coating has a strong wavelength dependence in the 8 to 12 μm wavelength range, as illustrated in Figure 2. However, this dependency becomes less significant as the detector module receives the integrated energy across the 8 to 12 μm range. Furthermore, the spatial or temporal brightness temperature profile allows for the identification of a solar flare and its magnitude in the MIR. The absorption due to SiO_2 was

Table 2. Optical characteristics in direct coupling.

$\varnothing_{tel}$ (mm)	f (mm)	$f/\#$	Res (arcsec pix^{-1})	FOV (arcmin)
72	1360	$f/19$	35	9.2×2.3

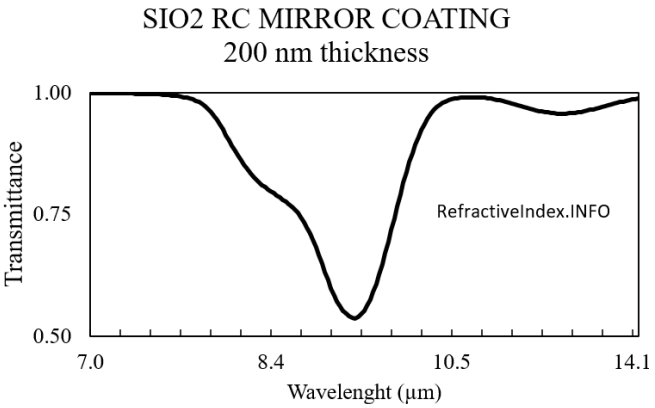

Figure 2. Optical transmission in the MIR range for the SiO_2 coating of the RC telescope mirrors. https://refractiveindex.info/?shelf=main&book=SiO2&page=Kischkat.

accounted for in the global transmittance of the atmosphere and the optical components of the telescope.

An aluminum cap was designed and built for placement at the telescope's aperture. The cap has two circular windows where optical filters with diameters smaller than the original opening of the telescope tube can be placed, as shown in Figures 3(a) and 3(b). Each opening had a diameter of 72 mm. In one of these, a germanium (Ge) window was installed. On the other hand, a neutral filter for visible-light observation was placed. The Ge window has a transmittance of 0.45 in the 2 to 15 μm wavelength range and is opaque to visible light radiation. It functions as a broadband filter in the MIR range. The MIR detector module was placed at the back focus (BF). The MIR detector module contains a second Ge window. Its function is to limit the electromagnetic spectrum band of MIR radiation to the wavelength band between 8 and 12 μm. The transmittance in this range was above 0.95 because of the coating on both sides of the window. Because the MIR detector is a module similar to an eyepiece form factor that can be installed in the telescope, another detector module with a filter in a different MIR band can be placed.

3. OPTICAL COUPLING

Several optical couplings are proposed in this section to fulfill the observational requirements of the TSP-MIR: 1) direct coupling, that is, the MIR detector module is placed at the focal plane of the RC telescope; 2) coupling using custom-made lenses between the telescope and the MIR detector module; 3) coupling using commercial catalog lenses; 4) coupling using a system of commercial catalog lenses; and 5) coupling using a configuration of custom-made mirrors. For each optical coupling, simulations were performed in Zemax, and the dispersion results in the spot diagram, point spread function (PSF), diffraction limit given by the Airy disk diameter, and effective focal ratio were analyzed. Additionally, the ease of integrating lenses or mirrors into a practical and functional optical coupling was considered in the analysis.

3.1. Direct coupling

Direct coupling is the configuration of the TSP-MIR in which the MIR detector module is placed at the focal plane of an RC telescope. This is the base configuration, as the Ge windows used in the direct coupling were also used in the other coupling configurations discussed later.

In direct coupling, two important values are considered: the pixel size of the detector and Airy disk. To achieve good telescope performance, the Airy disk at the focal plane must be similar in size to an individual pixel of the detector. The RC telescope has a focal ratio of $f/9$ and a pupil diameter of 150 mm. Therefore, at 10 μm, the Airy disk has an angular diameter of 16.5 arcsec or 0.11 mm at the focal plane of the telescope. Considering that the Airy disk is less than half the size of the detector pixel (0.23 mm), there is a margin for reducing the entrance pupil of the telescope. This reduced the cost of the Ge window placed in the telescope cap without affecting the image resolution. A Ge window of 72 mm diameter was selected, which also has the advantage of reducing the incident energy on the detector. With a 72 mm Ge window, the focal ratio is $f/19$, and the Airy disk has an angular diameter of 35 arcsec or 0.23 mm at the focal plane of the telescope, making it similar in size to a pixel of the detector. Table 2 lists the values of the telescope diameter and focal length, along with the resolution and FOV of the MIR detector module placed at the focal plane of the telescope. It is worth noting that observations in the MIR range are not entirely free from atmospheric turbulence or seeing; however, their impact becomes negligible, primarily due to two factors. First, the Fried coherence length, $r_0 \propto \lambda^{6/5}$, increases substantially at long wavelengths, approximately $30-60$ cm at 10 μm, thereby mitigating phase distortions induced by turbulence (Fried, 1966). Second, based on Roddier's model (Roddier, 1999), when the telescope diameter $\varnothing_{tel}$ is smaller than r_0, a condition frequently encountered in MIR observations, wavefronts retain spatial coherence, effectively minimizing the seeing effects. Consequently, the effective resolution in the MIR range is constrained by the diffraction limit of the telescope, rather than by atmospheric perturbations.

As mentioned earlier, the optics of the solar telescope include at least two refractive optical elements: the Ge window at the entrance pupil of the telescope and a smaller Ge window installed in the module detector. These two elements limit the light spectrum to a range between 8 and 12 μm and attenuate the energy reaching the detector to prevent pixel overheating. Assuming the Sun as a blackbody emitter, the energy reaching the detector is on the order of $E_{pixel} = 0.3{\times}10^{-6}$ J. This estimation considers the combined transmittance of the Ge windows and mirrors, atmospheric opacity, and internal obstructions of the RC telescope tube, integrated into the value of $\Gamma = 0.15$. At this energy, the temperature in a pixel is approximately 150 °C, which is within the operating range of the detector. Figure 4 shows the TSP-MIR modeled in Zemax with ray tracing of the direct-

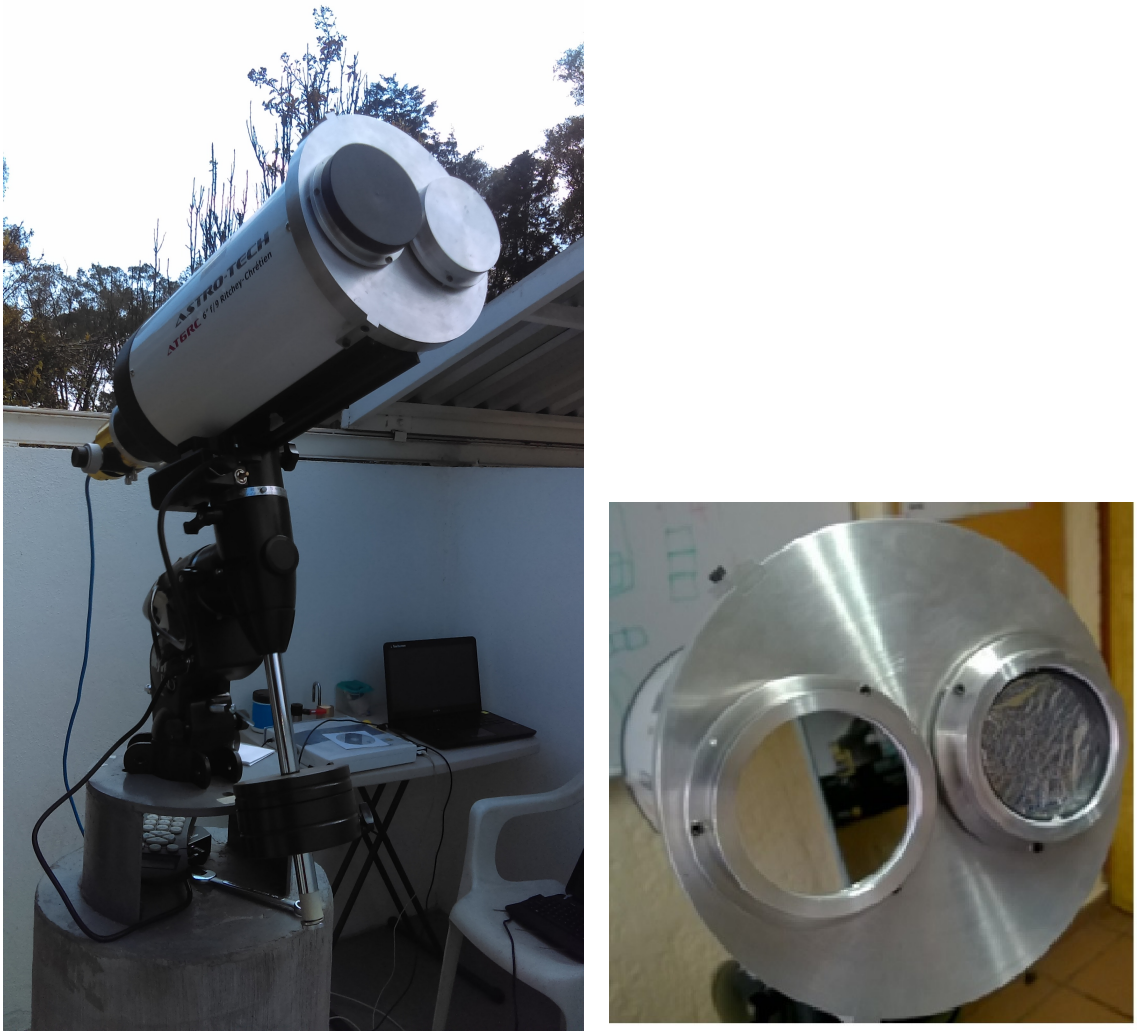

a b

Figure 3. (a) Ritchey-Chretien telescope with the filter cap. (b) Filter cap of the RC telescope. The filter on the left was made of a natural germanium crystal. It has an aperture of 72 mm. The window on the right is for the neutral filter for observing in visible light.

coupling configuration. The figure shows that the structure of the secondary mirror partially obstructs the optical path of the rays traced from the entrance pupil.

3.2. Optical Coupling to Expand FOV

Optical coupling between the RC telescope and the MIR detector was integrated to increase the observable area of the solar disk. The couplings studied in this work used lenses and mirrors. This study is based on the initial optical coupling between the telescope and detector, which increases the FOV achieved with direct coupling by a factor of three. Therefore, the new FOV provides coverage of $27' \times 6'$ for the solar observations. The coupling is an image reducer with two refractive elements made of Ge crystals, as shown in Fig. 5. The focal ratio of the RC telescope was initially $f/19$, calculated with a pupil diameter of 72 mm. With optical coupling that expands the FOV by a factor of three, the focal ratio of the system is reduced in the same proportion as $f/6.3$. The intermediate focal ratios of the lenses are shown in the image.

The initial optical configuration was simulated using Zemax software, which operates on geometric optics. The simulation used input parameters such as lens diameter, focal length, and refractive index. The area of the MIR detector was also considered, assuming that the detector was located in the focal plane of the system. The optimization of the initial optical coupling was performed using the size of the light-ray dispersion area at the

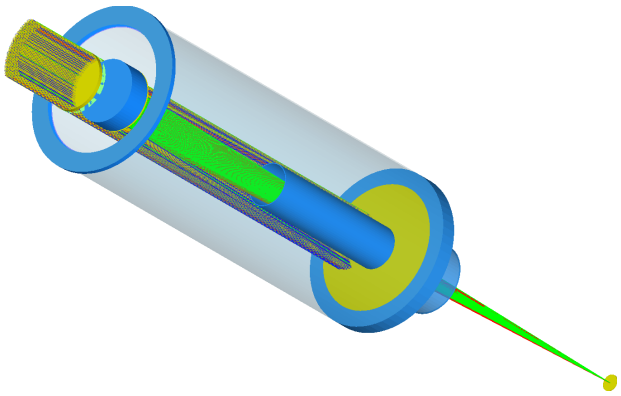

Figure 4. Model of TSP-MIR in the configuration of direct coupling with ray tracing performed in Zemax. The figure shows how the structure of the secondary mirror partially obstructs the light entry.

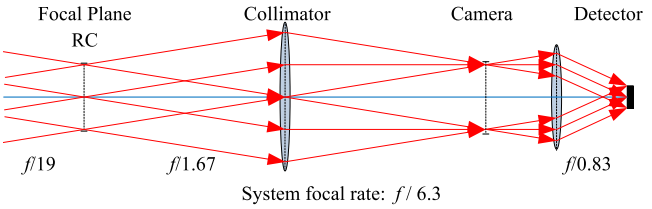

Figure 5. Model of the direct coupling with ray tracing performed in Zemax. The model was built using geometric optics and paraxial approximation.

focal plane of the system as a figure of merit. The optimized optical coupling is referred to as a custom-made lens. Couplings using catalog lenses, a system of catalog lenses, and a coupling system using custom-made mirrors were also simulated. For each coupling system, the following were calculated: First, the spot diagram at the principal ray was calculated, which allowed the aberration in the image detector plane to be determined and compared with the Airy disk diameter. In addition, the spot diagram at the maximum off-axis angle was calculated for each optical coupling to evaluate its performance. As each coupling has a distinct FOV, the maximum off-axis angles vary. This analysis provides insights into the image quality of the entire detector surface. Second, the Point Spread Function (PSF) describes the energy dispersion in the detector plane for a point source. From the PSF, one-dimensional profiles can be derived based on cross-sections in both the horizontal and vertical directions; and third, the Full Width at Half Maximum (FWHM) of the PSF cross-sections, which quantifies the energy dispersion. The FWHM should be comparable to or smaller than the Airy disk to preserve the resolution provided by diffraction limit.

4. RESULTS AND DISCUSSION

The optical couplings were optimized and simulated using Zemax software. The merit function used in the optimization minimizes the RMS of the diameter value for the spot diagram referenced to the principal ray. The goal was to ensure that the spot diagram diameter was smaller than the Airy disk diameter. The wavelengths used for the optimization and analysis were 8, 10, and 12 μm.

4.1. Direct coupling

As explained, in the direct coupling configuration, the MIR detector module is positioned at the focal plane of the RC telescope. A paraxial approximation was used to simulate the telescope mirror. For the Zemax simulation of the Ge windows, the thickness of each window was considered to being 5 mm for the window at the telescope aperture and 1 mm for the MIR detector module window. The refractive index of both windows was four. The optimization of the direct coupling was performed for the MIR detector position, aiming to achieve convergence of the rays at the detector plane. As a result, the dispersion in the spot diagram was concentrated in an area smaller than 1 μm, although the diameter of the Airy disk at 10 μm of wavelength ($\Phi_{10\mu m}$) is 465 μm. The $\Phi_{12\mu m}$ is 558 μm. Figure 6 shows the spot diagram for rays parallel to the optical axis. The spot diagram is similar for rays with off-axis angles in the X and Y directions. The small circle in the center of the diagram represents a tightly clustered spot that indicates minimal aberrations. The dashed line circumference represents

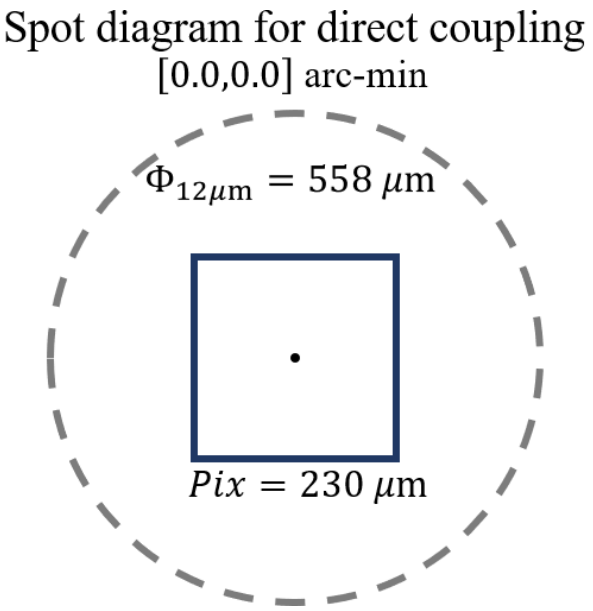

Figure 6. The spot diagram for direct coupling is shown for rays parallel to the optical axis of the telescope. The spot diagram is similar for rays with off-axis angles in the X and Y directions. The dashed line circumference represents the Airy disk at 12 μm with a diameter of 558 μm. The solid line square represents a pixel of the MIR detector, with a side length of 230 μm.

the Airy disk at 12 μm. The solid line square represents the area of the MIR detector pixel with sides of 230 μm in length.

Ideally, the PSF in the optical system should have a point-like or minimal dispersion within the wavelength range of 8 to 12 μm, remaining below the diffraction limit. For direct coupling, the PSF at a wavelength of 12 μm has an FWHM in the X direction of 463 μm and 217 μm in the Y direction, represented in Fig. 7(a) with solid and dashed lines. At wavelengths of 8 and 10 μm, the FWHM was smaller in both directions. The variation in width between the horizontal and vertical cross-sections arises from the off-center positioning of the Ge window installed in the telescope cap with respect to the optical axis. Moreover, the chromatic dispersion observed in the PSF across the wavelength range reduces the image resolution. Therefore, the analysis of the PSF for direct coupling and alternative configurations was focused on the 12 μm wavelength, as it exhibited the highest energy dispersion and lay within the detection range of the telescope. Figure 7(b) shows the PSF at the detector plane. The colors represent the magnitude of the normalized energy, with the red region having the highest magnitude and the blue region having the lowest. The oval shape of the PSF at the detector plane is a consequence of the position of the Ge window in the telescope cap. The image was superimposed on the circumference of the Airy disk. Similarly, a pixel of the MIR detector was represented in the model.

4.2. Optical Coupling with Individual Lenses: Custom and Catalog

To increase the field of view of the telescope for observing wide regions of the solar disk, an optical coupling design using custom-made lenses was proposed between the RC telescope and the MIR detector. A paraxial approximation and the well-known Gaussian lens formula were employed to calculate the diameter and radius of curvature of each plano-convex lens. The custom-

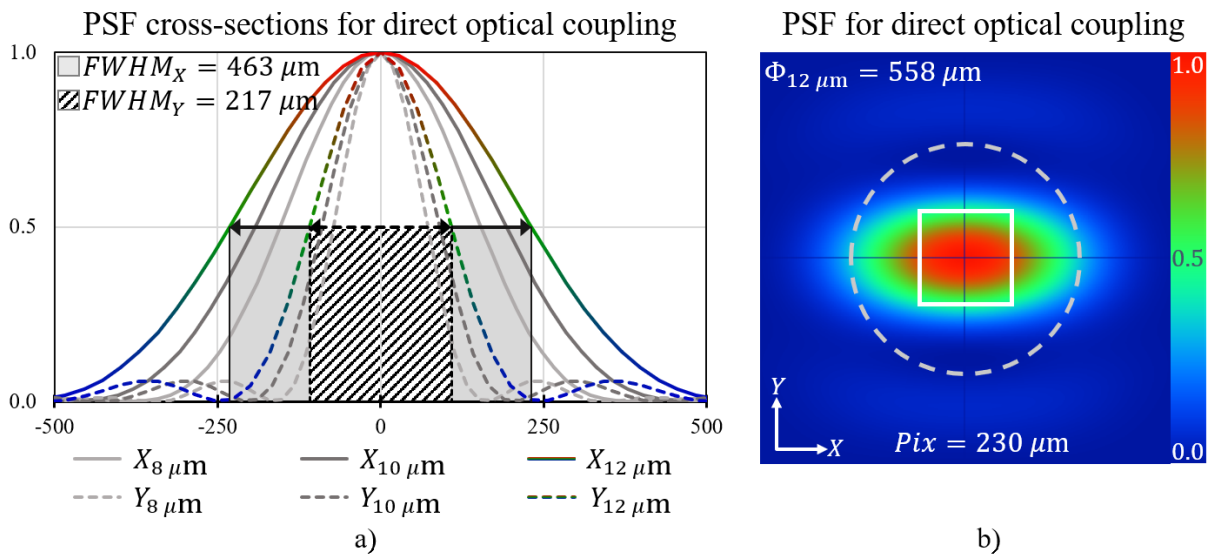

Figure 7. Analysis of the direct optical coupling between the telescope and the MIR detector. In (a), cross-sections of the PSF in the X direction (solid line) and the Y direction (dashed line) are shown. The region with continuous shading represents the FWHM of the PSF in the horizontal direction, and the region with striped shading represents the FWHM in the vertical direction. The FWHM in both directions for a 12 μm of wavelength is $FWHM_X = 463\ \mu$m and $FWHM_Y = 217\ \mu$m. The image in (b) corresponds to the PSF of the detector plane. The colors represent the intensity of the normalized energy, with red and blue indicating high and low magnitudes, respectively. The circumference represents the Airy disk at a wavelength of 12 μm. The solid line square represents a pixel of the MIR detector, with a side length of 230 μm.

made lens coupling was simulated in Zemax to optimize the distance between the lenses and the position relative to the back focus of the telescope, and the distance to the MIR detector. With this arrangement, the resulting effective focal ratio is $f/6.3$, and the detector's field of view is $27.7' \times 6.9'$. This FOV covers a region on the solar disk three times larger than that of direct coupling. The spot diagram obtained in the simulation for this coupling had a diameter smaller than that of the Airy disk, even for incident rays from the extreme angles of the FOV. Figure 8(a) shows the spot diagram for rays parallel to the optical axis, and 8(b) shows the spot diagram for off-axis rays with angles of -13.5′and 3′in the X and Y directions, respectively. In the same figures, the Airy disk is represented by the dashed line circumference and has a diameter of 184 μm at a wavelength of 12 μm. The Airy disk and spot diagram radii were smaller than the pixel size, as represented by the solid-line square.

An alternative version of the optical coupling uses lenses from the Edmund Optics catalog, with diameters and focal lengths similar to those proposed in the custom-made lens coupling design. The catalog lens coupling was simulated in Zemax, and it was found that the effective focal ratio was $f/5.8$ with a field of view of $30.1' \times 7.5'$. The region covered by this FOV was larger than that of the custom-made lens coupling and managed to cover the entire diameter of the solar disk in one direction. Figures 8(c) and 8(d) show the spot diagrams for the catalog. In Fig. 8(c), the spot corresponds to rays parallel to the optical axis of the telescope. As shown in Figure 8(d), the rays were angled at -13.5′and 3′in the X and Y directions. The Airy disk has a diameter of black169 μm at a wavelength of 12 μm. The Airy disk and spot diagram radii were smaller than the size of a pixel, which is represented by a solid line square.

Figures 9(a) and 9(c) show the PSF at a wavelength of 12 μm for the optical coupling with custom-made lenses and catalog lenses, respectively. By comparing the diagrams of the two couplings, it was observed that the energy was more concentrated with the catalog lens coupling than with the custom-made lens coupling. The FWHM in both the X and Y directions is smaller when coupled with the catalog lenses. Figures 9(b) and 9(d) show the 2D energy distributions of the PSF for both couplings. Their distribution is similar, although more concentrated with the coupling of catalog lenses. The Airy disk was larger with the catalog lens coupling than with the custom-made lens coupling. In any case, both the diffraction limit given by the Airy disk and the PSF distribution are smaller than the size of a pixel; therefore, the resolution of the telescope with either coupling is determined by the viewing angle of an individual pixel of the MIR detector.

4.3. Optical Coupling Using a Catalog Lens System

This section presents an analysis of optical coupling using a catalog lens system between the RC telescope and the MIR detector. The advantage of using a catalog lens system is that the manufacturer provides an optimized optical system that only needs to be placed at the back focus of the telescope. The focal ratio with this coupling is $f/8.9$, and its field of view is $19.6' \times 4.9'$. Figures 10(a) and 10(b) show the spot diagrams for incident rays parallel to the optical axis of the telescope and for rays with angles of -9.0′and 2.1′in the X and Y directions, respectively. The distances from the lens system to the telescope focus and from the lens system to the MIR detector were optimized using Zemax software. The shape and size of the spots at the two angles were significantly different, which could distort the image on the detector plane. The diameter of the Airy disk is 260 μm at a wavelength of 12 μm, which is larger than the pixel size of the MIR detector.

Figure 10(c) shows the PSF for coupling with the catalog lens system. The FWHM in the X direction is 213 μm (solid line), and in the Y direction is 102 μm (dashed line). Although the FWHM in both directions is smaller than a pixel of the MIR detector, part of the energy spreads beyond this limit. This is also observed in Figure 10(d), where the dispersion of the PSF exceeds the Airy disk and the pixel dimensions. Consequently, the image on the

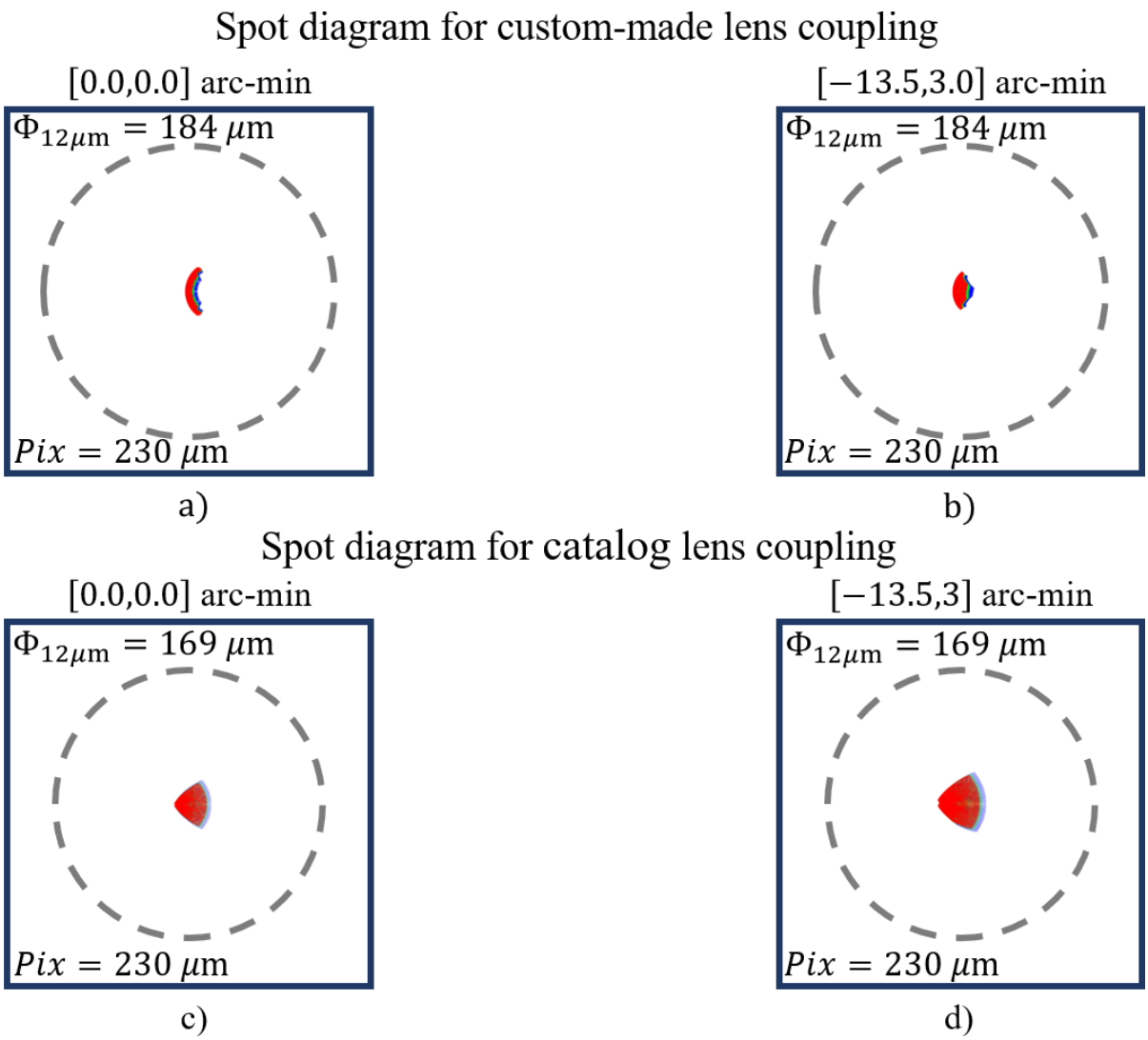

Figure 8. Representation of the spot diagram in the detector plane obtained in Zemax for the optical coupling using custom-made lenses and catalog lenses. Blue, green, and red represent 8, 10, and 12 μm wavelengths, respectively. The spot diagrams in (a) and (c) are for rays incident parallel to the optical axis of the telescope. The spot diagrams in (b) and (d) are for rays with incidence angles of -13.5′and 3.0′in X and Y directions, respectively. The dashed line circumference represents the Airy disk at 12 μm of wavelength. For the coupling with custom-made lenses, $\Phi_{12\ \mu m} = 184\ \mu m$; for the coupling with catalog lenses, $\Phi_{12\ \mu m} = 169\ \mu m$. The solid line square represents the size of a MIR detector pixel, with a side length of 230 μm.

detector plane has a poor resolution, which is determined by the PSF distribution.

4.4. Optical Coupling Using Custom-made Mirrors

Optical coupling using custom-made mirrors between the telescope and MIR detector was analyzed, as shown in Figure. 11. The advantage of using mirrors for optical coupling is their low energy absorption at mid-infrared wavelengths. The mirrors that formed the coupling were hyperbolic, and their surfaces were composed of aluminum. The coupling was optimized in Zemax for the radii of curvature of the mirrors and the distances between them. The results of the analysis performed using Zemax are shown in Figure 12. In Fig. 12(a), the spot diagram for the incident rays parallel to the optical axis of the telescope is shown. Figure 12(b) shows the rays at angles of -13.5′and 3.0′in the X and Y directions. The spot diagram exhibits an irregular distribution of ray-tracing on the detector plane. However, the spot sizes were smaller than the Airy disk for a wavelength of 12 μm, with $\Phi_{12\ \mu m}$ = 187 μm. In Fig. 12(c), the FWHM values in the horizontal and vertical directions are presented. In the horizontal direction, $FWHM_X = 155\ \mu m$, and in the vertical direction, $FWHM_Y = 72\ \mu m$. In both directions, the widths were smaller than the Airy disk and less than the area of a single detector pixel. Figure 12(d) shows the dispersion of the PSF on the plane, revealing a shift toward the right in the horizontal direction, which is attributed to the displacement of the entrance pupil. It is important to emphasize that most of the energy is concentrated within an area smaller than that of the detector pixels. This implies that the resolution of the telescope is determined by the pixel size, as previously expected.

5. Analysis of the Results

Table 3 lists the optical parameters used to characterize telescope performance. These include the focal ratio ($f/\#$), focal length (f), and field of view (FOV) of the camera. The diffraction limit, defined by the Airy disk at 12 μm, is also listed ($\Phi_{12\mu m}$). Additionally, the spot diameter for the chief rays is specified ($\varnothing_s$).

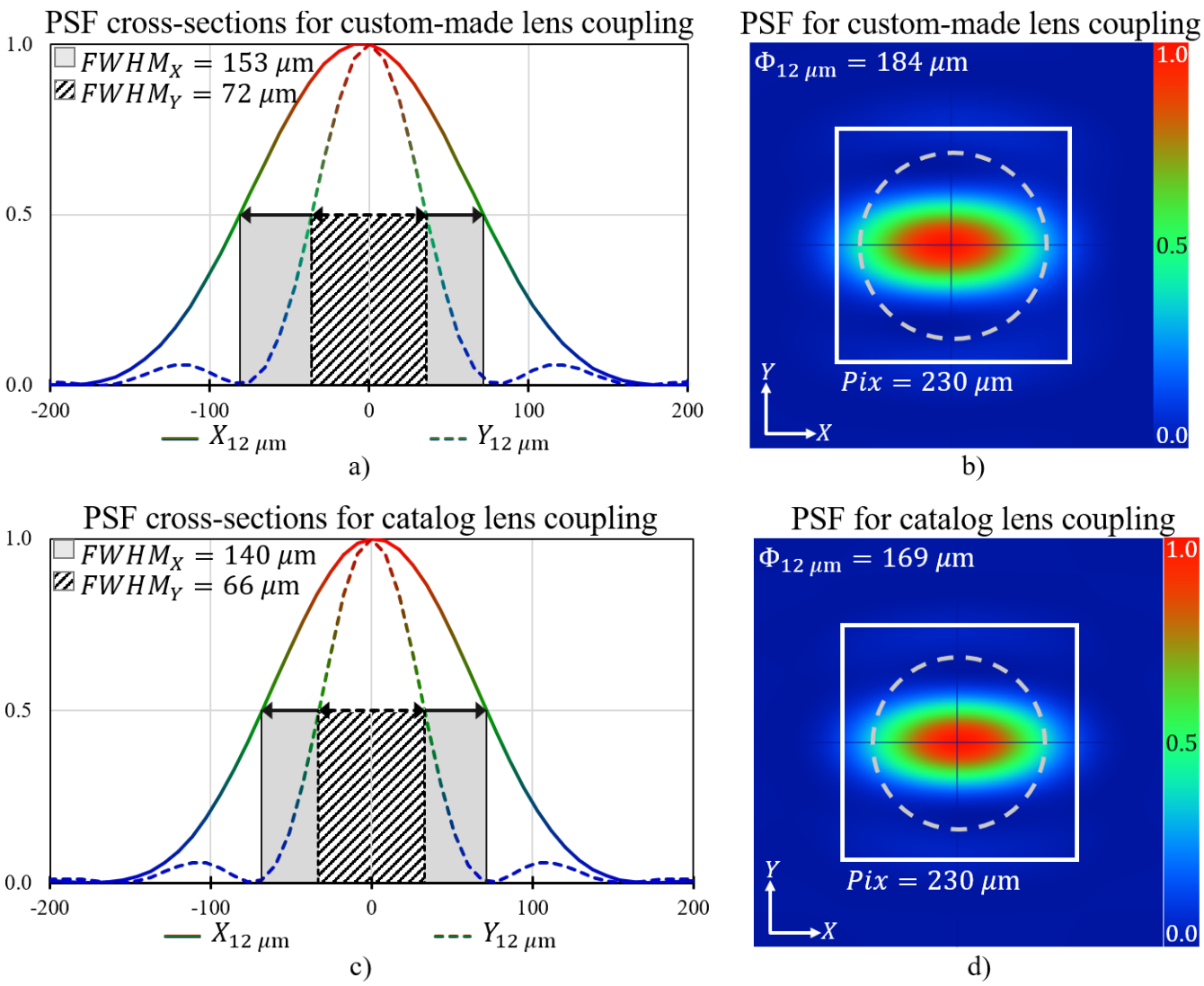

Figure 9. Analysis of the PSF for custom-made lenses and catalog lenses couplings. The figures in (a) and (c) are the cross-sections of the PSF in the X direction (solid line) and the Y direction (dashed line). The region with continuous shading represents the FWHM of the PSF in the horizontal direction, and the region with striped shading represents the FWHM in the vertical direction. The figures in (b) and (d) correspond to the PSF in the detector plane for couplings with custom-made and catalog lenses, respectively. The dashed line circumference represents the Airy disk, and the solid line square represents a pixel of the MIR detector, with a side length of 230 μm.

Table 3. Optical coupling parameters

Coupling	$f/\#$	f (mm)	ℓ_f (mm)	FOV (arcmin)	$\Phi_{12\mu m}$ (μm)	$\varnothing_s$ (μm)	$FWHM_X$ (μm)	$FWHM_Y$ (μm)
Direct	$f/19$	1370	0.0	9.2×2.3	558	$\geq$ 0.1	463	217
Custom-made lens	$f/6.3$	455	144	27.7×6.9	184	$\approx$ 32	153	72
Catalog lens	$f/5.8$	418	144	30.1×7.5	169	$\approx$ 42	140	66
Catalog lens system	$f/8.9$	657	235	19.6×4.9	260	$\approx$ 130	213	102
Custom-made mirrors	$f/6.3$	446	101	27.7×6.9	187	$\approx$ 148	155	72

Table 3 lists the FWHM of the PSF in the horizontal and vertical directions. The distance between the RC telescope focus and the MIR detector (ℓ_f) is given, with its value indicating the most compact and practical optical coupling for the TSP-MIR.

Inspection of Table 3 reveals superior optical performance in the three coupling configurations corresponding to the designs employing custom-made lenses, catalog lenses, and hyperbolic custom-made mirror. In each configuration, the FOV covered an area three times larger than that of the direct coupling arrangement. Additionally, the diffraction limit, defined by the Airy disk and energy distribution, is contained within the area corresponding to a single detector pixel, indicating that

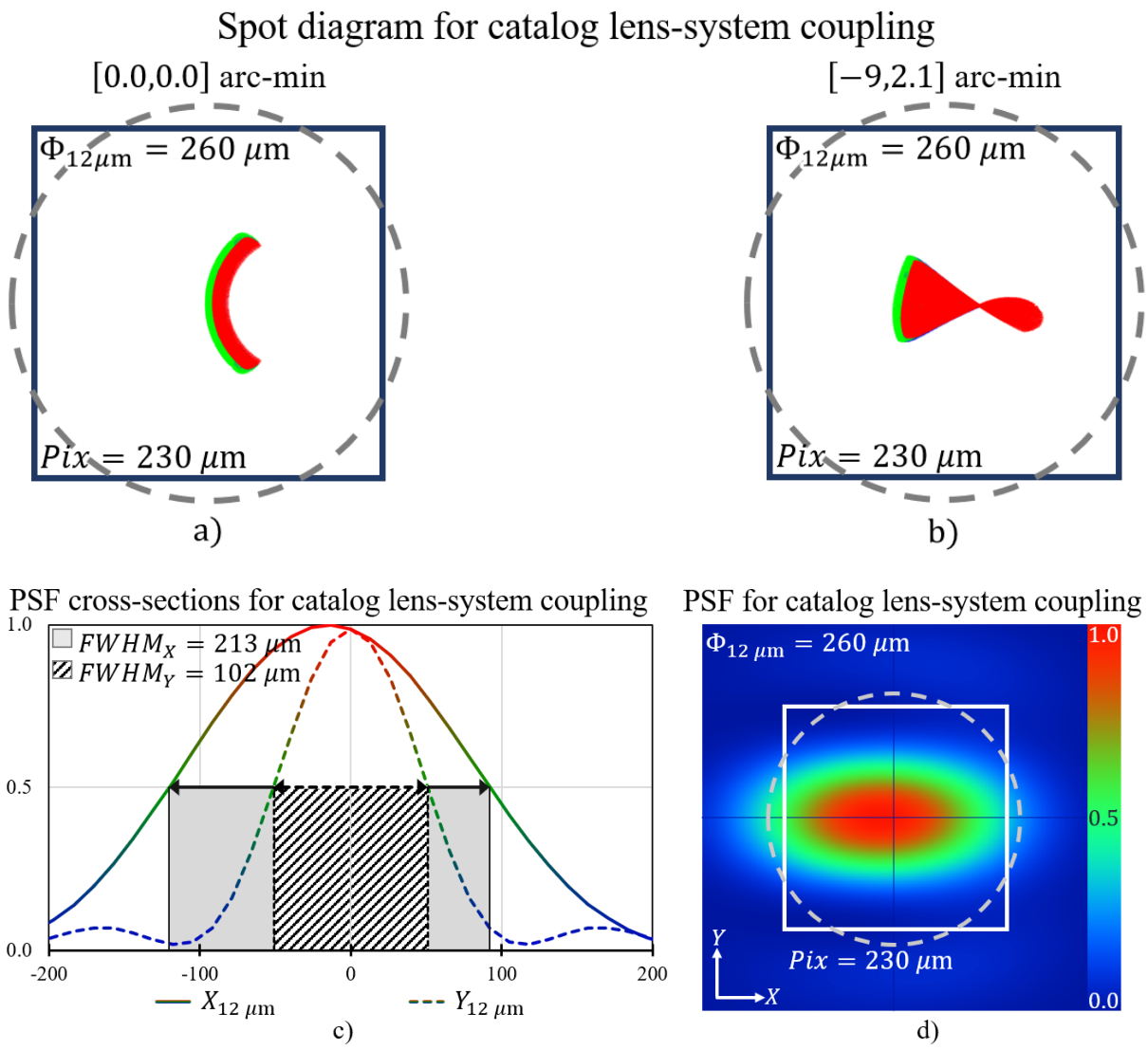

Figure 10. Analysis of the optical coupling using a catalog lens-system. In the upper panels, the spot diagrams for (a) rays parallel to the optical axis of the telescope and (b) rays with incidence angles of -9.0′and 2.1′in the X and Y directions, respectively, are shown. In (c), the curves of the cross-sections of the PSF in the horizontal and vertical directions with $\text{FWHM}_X = 213\ \mu$m (solid line) and $\text{FWHM}_Y = 102\ \mu$m (dashed line) are shown. In (d) represents the 2D energy distribution of the PSF on the detector plane. The dashed line circumference represents an Airy disk with a diameter of 260 μm. The solid line square represents a pixel of the MIR detector, with a side length of 230 μm.

the resolution is limited by the pixel size. Although these configurations met the same optical criteria, differences were noted in the spot diagram dimensions, with smaller spot sizes produced in the lens configurations, which resulted in reduced image distortion at the detector plane. Finally, the coupling design using catalog lenses was assembled with a smaller physical volume than the other alternatives.

Considering the optical parameters summarized in Table 3, it was determined that the configurations using custom-made and catalog lenses offered the most significant advantage in expanding the telescope's field of view. Finally, considering the ease of implementing optical coupling, it was found that catalog lens coupling is the best alternative for achieving the proposed optical objectives for the TSP-MIR.

6. Conclusions

The size of the spots on the detector plane and energy dispersion are two quantities that characterize the quality of an image. In this study, the custom-made lens coupling did not exhibit better characteristics than the catalog lens coupling. However, coupling with a catalog lens system results in poor performance and is not recommended. Hyperbolic custom-made mirrors offer comparable performance to custom-made lenses but are more difficult to manufacture and align within the coupling system. Therefore, considering the FOV and other simulated parameters, optical coupling using catalog lenses is the most suitable for installation in the TSP-MIR. Direct coupling has a smaller FOV than that of coupling with catalog lenses. However, its field of view is useful for observing individual active regions at higher resolutions. Owing to their ease of integration with catalog lenses

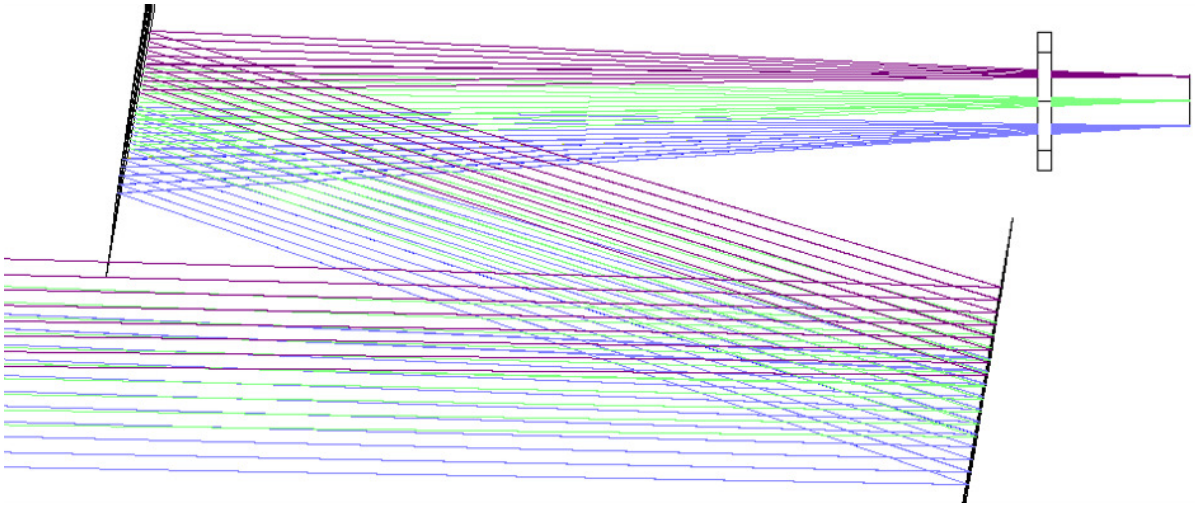

Figure 11. Optical coupling configuration using custom mirrors. The surface of the mirrors is aluminum, and their curvature is hyperbolic.

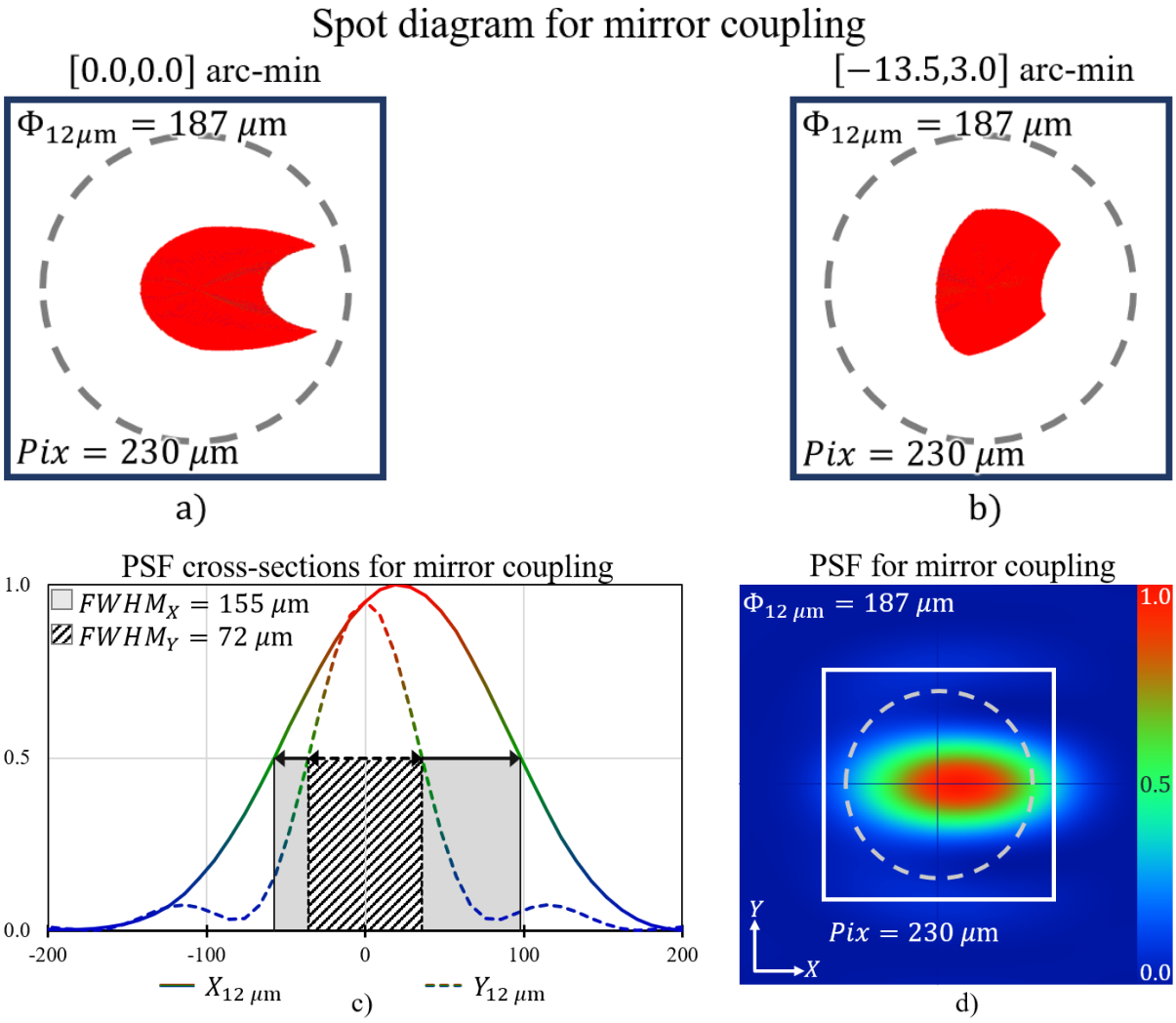

Figure 12. Analysis of the optical coupling using custom-made mirrors. In the upper panels, the spot diagrams of the diffraction pattern for (a) rays parallel to the optical axis of the telescope and (b) rays with incidence angles of -13.5′and 3.0′in the X and Y directions, respectively, are shown. In (c), the curves of the PSF cross-sections in the horizontal and vertical directions with $FWHM_x = 155\ \mu$m and $FWHM_y = 72\ \mu$m are shown. In (d) represents the 2D energy distribution of the PSF on the detector plane. The dashed line circumference corresponds to the Airy disk with a diameter of $\Phi_{diff} = 187\ \mu$m. The solid line square represents a pixel of the MIR detector, with a side length of 230 μm.

and direct coupling, these configurations can be replicated in other telescopes and used individually to observe different regions of the Sun.

REFERENCES

Aschwanden, M. J. 2006, Physics of the Solar Corona, 1th ed. (Berlin, Heidelberg: Springer)

Forbes, T. G. 2000, RSPTA, 358, 711, doi: 10.1098/rsta.2000.0554

Fried, D. L. 1966, JOSA, 56, 1372, doi: 10.1364/JOSA.56.001372

García-Lorenzo, B., Eff-Darwich, A., Castro-Almazán, J., et al. 2010, MNRAS, 405, 2683, doi: 10.1111/j.1365-2966.2010.16649.x

Giménez de Castro, C. G., J.-P., R., Valle Silva, J. F., et al. 2018, SpWea, 16, 1261, doi: 10.1029/2018SW001969

Giovanelli, R., Darling, J., Henderson, C., et al. 2001, PASP, 113, 803, doi: 10.1086/322136

Hills, R., & Richer, J. 2000, Water Vapour Radiometers for ALMA, Tech. rep., National Radio Astronomy Observatory. https://library.nrao.edu/public/memos/alma/main/memo303.pdf

Hudson, H. S., & Lindsey, C. A. 1974, ApJ, 187, L35, doi: 10.1086/181386

Judge, P., Tomczyk, S., Hannigan, J., & Sewell, S. 2019, A, 877, 10, doi: 10.3847/1538-4357/ab0e04

Kaufmann, P., Levato, H., Cassiano, M. M., et al. 2008, in Society of Photo-Optical Instrumentation Engineers (SPIE) Conference Series, Vol. 7012, Ground-based and Airborne Telescopes II, ed. L. M. Stepp & R. Gilmozzi, 70120L, doi: 10.1117/12.788889

Kaufmann, P., Abrantes, A., Bortolucci, E. C., et al. 2012, in Society of Photo-Optical Instrumentation Engineers (SPIE) Conference Series, Vol. 8442, Space Telescopes and Instrumentation 2012: Optical, Infrared, and Millimeter Wave, ed. M. C. Clampin, G. G. Fazio, H. A. MacEwen, & J. M. Oschmann, Jr., 84424L, doi: 10.1117/12.926072

Kaufmann, P., White, S. M., Freeland, S. L., et al. 2013, ApJ, 768, 134, doi: 10.1088/0004-637x/768/2/134

Kaufmann, P., Marcon, R., Abrantes, A., et al. 2014, ExA, 37, 579, doi: 10.1007/s10686-014-9389-y

Kaufmann, P., Abrantes, A., Bortolucci, E. C., et al. 2016, in 2016 41st International Conference on Infrared, Millimeter, and Terahertz waves (IRMMW-THz), 1–2, doi: 10.1109/IRMMW-THz.2016.7758395

Kischkat, J., Peters, S., Gruska, B., et al. 2012, ApOpt, 51, 6789, doi: 10.1364/AO.51.006789

Lindsey, C., & Heasley, J. 1981, ApJ, 247, doi: 10.1086/159043

López, F. M., Giménez de Castro, C. G., Mandrini, Cristina H., et al. 2022, A&A, 657, A51, doi: 10.1051/0004-6361/202141967

Marcon, R., Kaufmann, P., Melo, A. M., Kudaka, A. S., & Tandberg-Hanssen, E. 2008, PASP, 120, 16, doi: 10.1086/525058

McIntosh, P. S. 1990, SoPh, 125, 251, doi: 10.1007/BF00158405

Melo, A. M., Kaufmann, P., Kudaka, A. S., et al. 2006, PASP, 118, 1558, doi: 10.1086/509267

Naylor, D. A., Chapman, I. M., & Gom, B. G. 2002, in Society of Photo-Optical Instrumentation Engineers (SPIE) Conference Series, Vol. 4815, Atmospheric Radiation Measurements and Applications in Climate, ed. J. A. Shaw, 36, doi: 10.1117/12.482317

Otárola, A., Travouillon, T., Schöck, M., et al. 2010, PASP, 122, 470, doi: 10.1086/651582

Penn, M., Krucker, S., Hudson, H., et al. 2016, ApJL, 819, L30, doi: 10.3847/2041-8205/819/2/L30

Pierce, A. K. 1969, SoPh, 6, 498, doi: 10.1007/BF00146486

Polyanskiy, M. 2021, Refractive Index Database. https://github.com/polyanskiy/refractiveindex.info-database

Qin, Z., Karnieli, A., & Berliner, P. 2001, IJRS, 22, 3719, doi: 10.1080/01431160010006971

Riedl, G. 2009, Optical Desing, Applying the Fundamentals, Tutorial texts in optical engineering (Bellingham, Washington: SPIE press), doi: 10.1117/3.835815

Roddier, F. 1999, Adaptive Optics in Astronomy (Cambridge, UK: CUP)

Sobrino, J., Jiménez-Muñoz, J.-C., & Paolini, L. 2004, RSEnv, 90, 434, doi: 10.1016/j.rse.2004.02.003

Turon, P. J., & Léna, P. J. 1970, SoPh, 14, 112, doi: 10.1007/BF00240164